Hindawi
Advances in Materials Science and Engineering
Volume 2017, Article ID 2808262, 9 pages
https://doi.org/10.1155/2017/2808262

Research Article

Preparation, Characterization, and Evaluation of Humidity-Dependent Electrical Properties of Undoped and Niobium Oxide-Doped $TiO_2 : WO_3$ Mixed Powders

Pedro M. Faia,[1] Juliano Libardi,[2] Itamar Barbosa,[3] Evando S. Araújo,[4] and Helinando P. de Oliveira[4]

[1]*CEMUC, Electrical and Computers Engineering Department, Faculty of Sciences and Technology, University of Coimbra, Polo 2, Pinhal de Marrocos, 3030-290 Coimbra, Portugal*
[2]*Physics Department, Technological Institute of Aeronautics (ITA), Pça. Marechal Eduardo Gomes 50, 12228-900 São José dos Campos, SP, Brazil*
[3]*Industrial Fostering and Coordination Institute (IFI), Pça. Marechal Eduardo Gomes 50, Vila das Acácias, São José dos Campos, SP, Brazil*
[4]*Institute of Materials Science, Federal University of Sao Francisco Valley, 48920-310 Juazeiro, BA, Brazil*

Correspondence should be addressed to Evando S. Araújo; evando.araujo@univasf.edu.br

Received 22 June 2017; Revised 28 August 2017; Accepted 11 September 2017; Published 13 December 2017

Academic Editor: Charles C. Sorrell

The study of selective metal oxide-based binary/ternary systems has received increasing interest in recent years due to the possibility of producing efficient new ceramic materials for relative humidity (RH) detection, given the superior properties of the mixed compounds in comparison with pristine ones. The aim of this work was focused on preparation and characterization of non-doped and Nb_2O_5-doped $TiO_2 : WO_3$ pair (in the pellet form) and evaluation of corresponding humidity-dependent electrical properties. The microstructure of the samples was analyzed from scanning electron microscopy, X-ray diffraction patterns, Raman spectra, BET surface area analysis, and porosimetry. The electrical characterization was obtained from impedance spectroscopy (100 Hz to 40 MHz) in the 10–100% RH range. The results showed that adequate doping levels of Nb_2O_5 introduce important advantages due to the atomic substitution of Ti by Nb atoms in highly doped structures with different levels of porosity and grain sizes. These aspects introduced a key role in the excursion (one order of magnitude) in the bulk resistance and grain boundary resistance, which characterizes these composite ceramics as a promising platform for RH identification.

1. Introduction

The development of new ceramic metal oxide materials provides a promising platform for diverse applications such as optoelectronics, microelectronics, dye-sensitized solar cells, and tunneling devices [1–3].

In particular, the production of moisture sensors of metal oxide materials requires improved selectivity and stability for water sorption. These processes are intrinsically dependent on microstructure and prevailing transport mechanisms of resulting materials. The doping process induced by metal oxides introduces atomic defects which affect the overall conduction mechanisms of blends, characterizing the relative concentration of a dopant as a tuning parameter in the optimization of electrical response in terms of RH variation [4–7].

The typical process of structural modification is provided by mechanical mixing of the powders, molding, and sintering of the pelletized samples [8, 9].

The introduction of a doping agent in a mixed metal oxide ceramic has been considered an interesting strategy for improvement in the dependence of impedance value with relative humidity (RH) variation [10–13]. The incorporation of dopants affects the structure and morphology of the ceramic, providing additional path-structural water layer interaction.

In this work, the authors explored the incorporation of niobium pentoxide (Nb_2O_5)—an n-type transition metal oxide (E_g of 3.2–4 eV) applied as a dopant for the $TiO_2 : WO_3$ pair. The microstructure was evaluated from SEM images, X-ray diffraction patterns, Raman spectra, BET analysis, and porosimetry. These techniques were explored in order to evaluate the influence of each component on the overall electrical response of the blends under controlled variation of RH.

2. Experimental

2.1. Materials and Methods. TiO_2, WO_3, and Nb_2O_5 (Fluka) were used as received. Grain size was determined using an Autosizer II C (Malvern Instruments). The X-ray diffraction patterns were obtained by means of a Philips X'Pert, PW 3040/00 using Cu-K_α radiation ($K_\alpha = 1.5418$ Å) ($20^\circ < 2\theta < 75^\circ$) with 0.04° of step and 0.5 s per point. Raman spectra of the samples were obtained in a HORIBA Jobin-Yvon Raman spectrometer in which the excitation wavelength was adjusted to 532 nm with a power of 25 mW. SEM images were obtained in a Philips scanning electron microscope (model XL 30 TMP), operated at 30 kV. The pore area was determined using a Micromeritics PoreSizer 9320 mercury porosimeter (as a standard procedure, chamber containing the samples was degasified, and then, mercury intrusion pressured analysis was performed in the pressure range from 0.5 up to 30000 psi). Brunauer–Emmett–Teller (BET) surface area experiments were provided by a Micrometrics ASAP using nitrogen gas. The impedance of the samples was measured in the range between 100 Hz and 10 MHz, with an AC voltage of 0.5 V—no bias, in a Hewlett-Packard (model HP4294A) impedance/gain-phase analyzer.

The experimental setup for impedance measurements consists in a 6.5-liter chamber in which the temperature is controlled with a 1°C precision in response to the RH variation with steps of 10% in an overall range from 10 to 100%. All the experiments were performed at 20°C. The RH values were obtained by mixing water-saturated air and dry synthetic air, in which the respective amount of each part was regulated by mass flow controllers. The impedance spectra for each RH value were reached at a continuous flow rate of 5 l/h, after at least 90 minutes of stabilization. The measuring electrical contacts were made of gold on opposite sides of the top surface of the samples.

2.2. Preparation of the Samples. The pristine $TiO_2 : WO_3$ powder was prepared by mechanical mixing of TiO_2 and WO_3 in the ratio of 48.92 : 51.08 wt.%, respectively. The dopant (Nb_2O_5) was incorporated by direct mixing with specific amounts (2, 4, and 6 wt.%), and named as TiW-Nb2, TiW-Nb4, and TiW-Nb6 samples. All the samples were prepared in the form of pellets for the microstructural and electrical characterization. The mixtures (pristine and doped powders) were initially pelletized in the samples of 8 mm × 6 mm × 1 mm under 8 MPa of uniaxial pressure and then isostatically pressed at 200 MPa. Afterwards, the thermal treatment (under air) was conducted at 700°C for 2 h with heating and cooling rates of 20°C/min in accordance with a previous used procedure [8, 9].

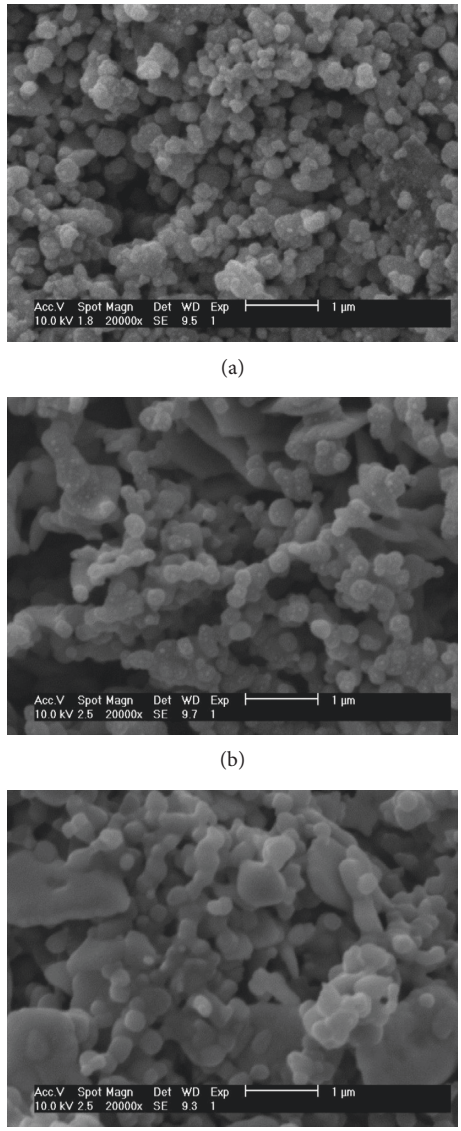

Figure 1: SEM micrographs of the $TiO_2 : WO_3$-doped sensors with 2% (a), 4% (b), and 6% (c) content of Nb_2O_5.

3. Results and Discussion

3.1. Morphology of the Mixed Pellets. SEM images of TiW-Nb2, TiW-Nb4, and TiW-Nb6 are shown in Figure 1. As can be seen, the resulting material is characterized by a porous surface with a distribution of different aggregation sizes of particles disposed in overlaid layers, providing free sites for molecule percolation along the structure. Statistical analysis of the images indicates a distribution of smaller grains with size around 225.4 ± 88.2 nm. A slight increase in the size of the smaller aggregates is observed for TiW-Nb4 sample, reaching 284.5 ± 131.6 nm. The aggregation level is favored by the

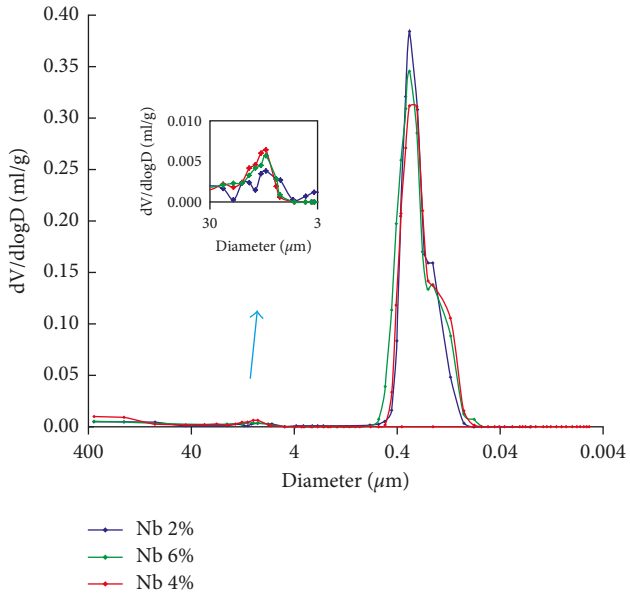

Figure 2: Log differential intrusion as a function of pore diameter of the TiO_2 : WO_3-doped samples with 2, 4, and 6% of Nb_2O_5 (inset: macropore region zoom).

progressive incorporation of a doping agent (Figure 1(c)) (TiW-Nb6 reveals aggregates with a diameter of about 386.7 ± 252.3 nm). By comparing the images, it is possible to identify a slight dependence of the aggregation level on the dopant concentration.

These data can be confirmed by the differential mercury intrusion curves (shown in Figure 2). As shown, a broad peak in the range of 0.07–0.5 μm with maximum in 0.275 μm is observed for all the samples. A weak contribution is observed in the range of 3–30 μm, shown in details in the inset, characterizing the distribution of aggregates with different sizes, as observed in the previous SEM images. Using the total volume of intruded mercury, the corresponding values for the total porosity were calculated: percentages of 34.4, 37.1, and 37.0 were determined for the samples TiW-Nb2, TiW-Nb4, and TiW-Nb6, respectively, indicating that doping load introduces minimal differences on the pore structure of the resulting material, which remain distinct due to the previously defined ratio of the semiconductors used in the preparation, preserving the structural humidity properties of the template.

The BET surface area of samples is summarized in Table 1. The results (Table 1) confirm that progressive incorporation of the dopant until 4 wt.% introduces negligible influence on the surface area of samples. The higher level of the dopant in the sample TiW-Nb6 affects the response (32% in terms of undoped ones) affecting the water adsorption if compared with samples prepared under low doping level condition.

3.2. Microstructural Characterization. The X-ray diffraction patterns of a pristine sensor (mixed TiO_2 : WO_3) sintered at

Table 1: BET surface area and crystal dimensions calculated from Scherrer's equation.

Samples	BET surface area (m^2/g)	Crystallite size (nm)	
		TiO_2	WO_3
TiW	5.15	20.8	19.5
TiW-Nb2	4.99	19.5	18.0
TiW-Nb4	4.94	20.1	18.5
TiW-Nb6	3.49	19.5	19.5

700°C for 120 minutes in air are compared with those of a nonsintered sample in the inset of Figure 3(a). It is noteworthy that the anatase phase of the nonsintered sample is converted into rutile phase as a consequence of annealing. Both TiO_2 polymorphs are characterized by tetragonal configuration consisting in TiO_6 octahedra that share four edges with anatase and two with rutile. The rutile is identified by the ICDD card no. 21-1276 according to the following crystal system: tetragonal space group: $P4_2/mmm - D_{4h}^{14}$ with the unit cell parameters $a = b = 4.5933$ Å and $c = 2.9592$ Å. The spectrum of tungsten trioxide, shown in the inset (B) of Figure 3(a), reveals the decrease in the intensity of the initial monoclinic phase due to the sintering process—by introduction of impurities and defects. It is also noticeable the appearance of the anorthic phase identified by ICDD card no. 083-0951 and of the monoclinic identified by ICDD card no. 071-0131. These diffraction patterns confirm the existence of a polycrystalline material that results from a mixture between the oxides. In Figures 3(b)–3(d), the XRD patterns of the samples TiW-Nb2, TiW-Nb4, and TiW-Nb6 are shown. The possible incorporation of Nb^{5+} ions into the crystalline structure of TiO_2 [14–16] can be assumed, once the corresponding ionic radius of Ti^{4+} and Nb^{5+} can be identified as a source for the absence of niobium peaks in the corresponding curves. The insets of Figures 3(b)–3(d) confirm the absence of the rutile phase and the incorporation of Nb atoms into the TiO_2 structure. XRD peaks of anatase TiO_2 were identified at $2\theta = 25.3°$, 36.9°, 37.8°, 38.5°, 48.1°, 55.1°, 62.7°, and 68.6°. The latter phase also has tetragonal organization with the space group D_{4h}^{19} $I4_1$ and with the unit cell parameters $a = b = 3.7842$ Å and $c = 9.5146$ Å, all identified by the ICDD card no. 21-1272. Therefore, in order to state more clearly the substitution of Ti atoms by Nb atoms, the unit cell parameters of samples under study were calculated from the anatase peaks located at $2\theta = 25.28°$ and $2\theta = 48.05°$. The calculated cell parameters are $a = b = 3.7818$ Å and $c = 9.6261$ Å for the sample TiW-Nb2, corresponding to an increase along c-direction and a decrease along a-b directions, when compared with the standard values. Such distortions reinforce the niobium incorporation: they were also observed for the sensors doped with 4 wt.% ($a = b = 3.7822$ Å and $c = 9.5971$ Å) and 6 wt.% ($a = b = 3.7838$ Å and $c = 9.5410$ Å). Moreover, the anatase phase showed a slight shift towards smaller 2θ angles as doping content increased, as verified in the changes in the peak positions $2\theta = 48.08°$ (2 wt.%) and $2\theta = 48.05°$ (6 wt.%). The average crystallite size of WO_3 and TiO_2 of doped and nondoped sensors was calculated

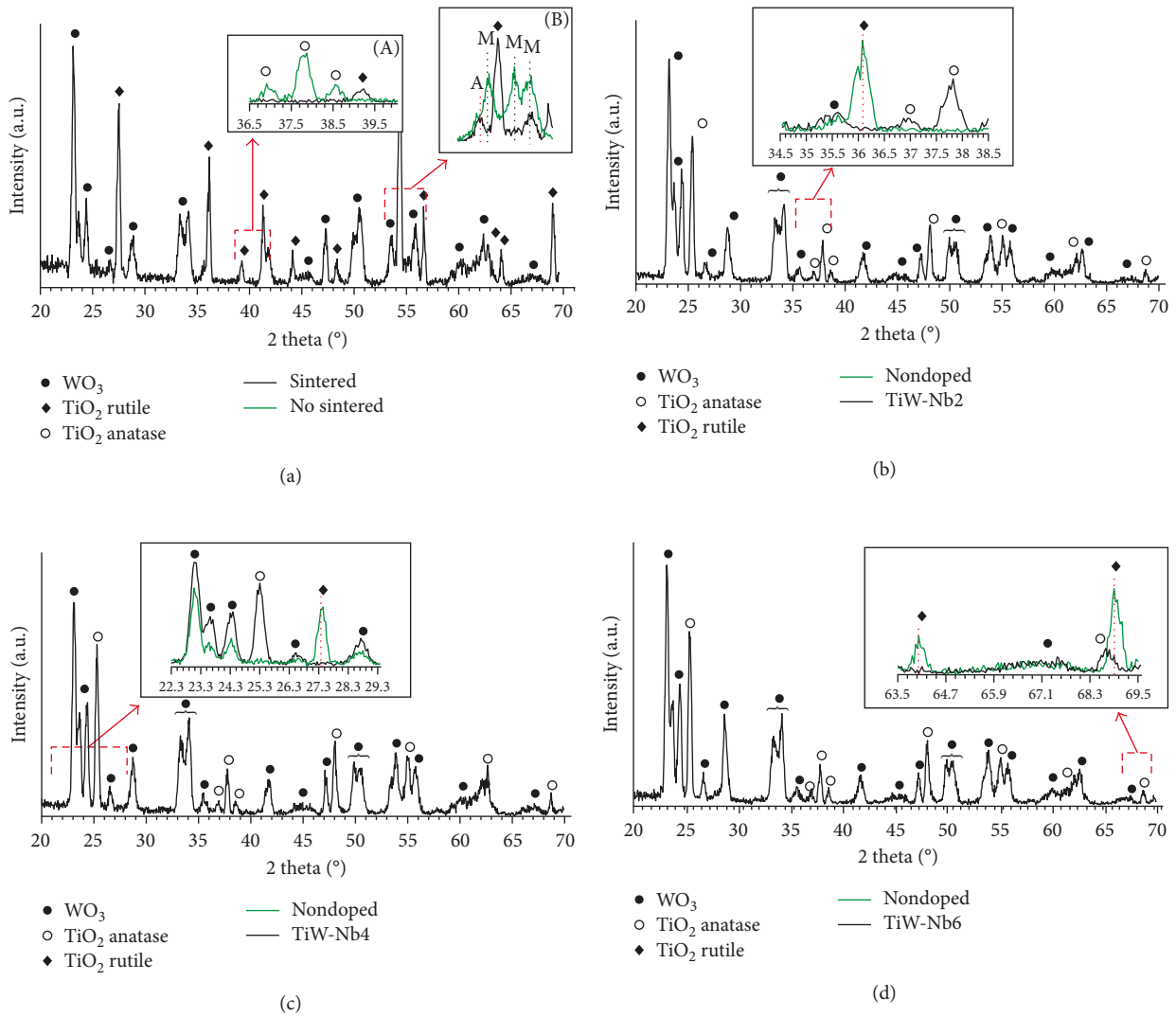

FIGURE 3: Diffraction patterns of a nondoped sensor (a) and of the TiO_2 : WO_3-doped sensors with 2% (b), 4% (c), and 6% (d) of Nb_2O_5.

by the Scherrer equation ($D = k.\lambda/\beta.\cos\theta$, where D denotes the crystallite size, β corresponds to the full width at half maximum, θ is the Bragg peak, in radians, λ is the wavelength of incident radiation, and k is the Scherrer constant). Table 1 summarizes the values obtained for the higher intensity reflections (101) and (002) of the TiO_2 and WO_3, respectively. Comparing both WO_3 and TiO_2 crystallite sizes of doping sensors with the value of nondoped sensor, it is observable that niobium incorporation promoted a slight decrease of crystallite dimensions for both oxides. These results indicate that niobium has been incorporated into the crystal lattice of titanium and provides considerable changes in the electrical response to humidity of the pellets.

The Raman spectrum of nondoped TiO_2 : WO_3 and TiW-Nb2 samples is compared in Figure 4(a). The incorporation of niobium originates a less intense peak in the spectrum, corresponding to the position at 635 cm^{-1}, and two other even less intense peaks at 513 and 390 cm^{-1}, attributed to the anatase phase, confirming that niobium hinders the phase change of titanium dioxide. The peak at 440 cm^{-1} in the spectrum of doped pellet is assigned to tungsten trioxide ($W^{5+} = O$), also visible in the Raman spectra of TiW-Nb4 and TiW-Nb6 (Figure 4(b)). The asymmetric shoulder formed is more evident for the higher doped sensor and might be associated with the proximity of the monoclinic WO_3 (mode G) vibrational mode at 605 cm^{-1} [17, 18].

3.3. Electrical Impedance Characterization of Samples. Electrical impedance spectroscopy has been progressively reported in the literature as a promising tool applied in the identification of phase transitions in materials [19–22] and transport mechanisms in structures of solid state (ceramics) and soft matter. The frequency-dependent excitation provides information about transport and polarization (transport, ionic diffusion, and charge separation). The graphical representation (Nyquist diagrams) offers a direct visualization of the different

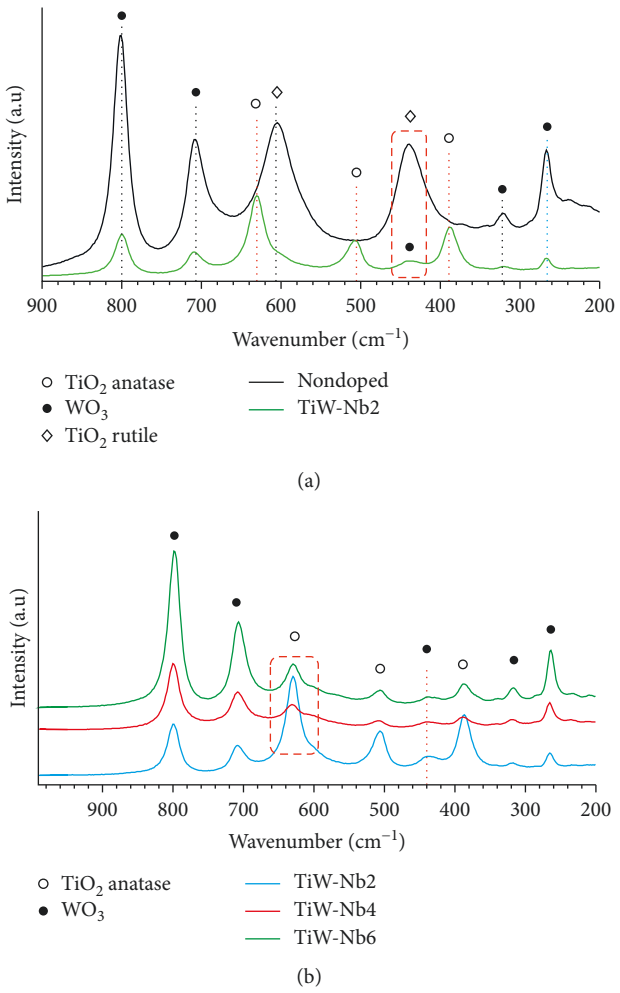

FIGURE 4: Raman spectra of the TiO_2 : WO_3-doped sensors: (a) nondoped and the 2% weight doped sensors; (b) 2, 4, and 6% content of Nb_2O_5.

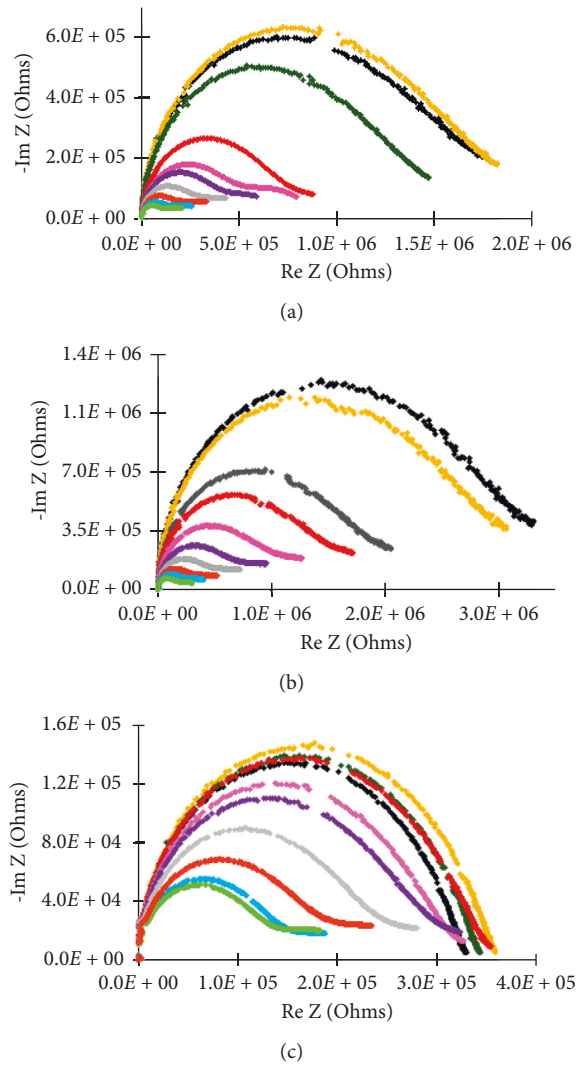

FIGURE 5: Nyquist plots at 20°C for the samples TiW-Nb2 (a), TiW-Nb4 (b), and TiW-Nb6 (c) (black, orange, dark green, brown, rose, purple, grey, red, light blue, and light green stand for 10, 20, 30, 40, 50, 60, 70, 80, 90, and 100% RH).

mechanisms (relaxation process—from a characteristic semicircle—and diffusion—from a straight line at low-frequency limit) [23].

In terms of surface conductivity in ceramics due to the progressive water adsorption [24], three different mechanisms are present [25]. At low RH range, the monomolecular adsorption process takes place as a response to surface modification due to water molecule incorporation, reaching a first complete layer, the chemisorbed one, in the range 20 to 40% RH. Above 40% RH, the proton conductivity of water dominates and diffusion effects tend to be more effective, improving the surface conductivity. The continuous formation of water layers, physisorbed ones, favors the ionic transport participation in the overall conduction process. The porous structure tends to be filled by water molecules, allowing proton transport between adjacent water molecules. With the increasing water adsorption rate, the surface conductivity tends to assume a constant value. Nyquist diagrams in Figures 5(a) and 5(b) reveal that a minimal variation is observed for all the samples if the considered RH concentration is above 70%, confirming the previous analysis; below 70% RH, the relaxation dominates over diffusion and two overlapping semicircles are present. At increasing RH (in the range of 40%–60%), diffusion contributions are added to the surface contribution due to the tunneling process along water layers. Above 70% RH, diffusion tends to be the dominant mechanism—as a result of mutual contribution of surface water layer and bulk water-filled pores. This pronounced behavior is similarly observed for the sample TiW-Nb4 (Figure 5(b)). Increasing dopant concentration affects the dependence of the electrical spectrum with RH variation. As expected, the minimal variation in the Nyquist curves' characteristic diameter reveals that saturation in the transport is reached.

These results are confirmed in Figure 6 (impedance measured at $f = 1.3$ kHz and 4 kHz, at 20°C for different doping levels). As shown, the incorporation of niobium in the composite reduces the range of variation of resulting

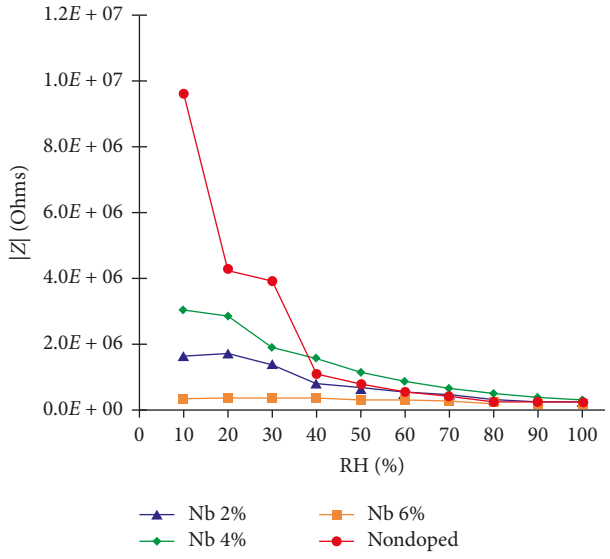

(a)

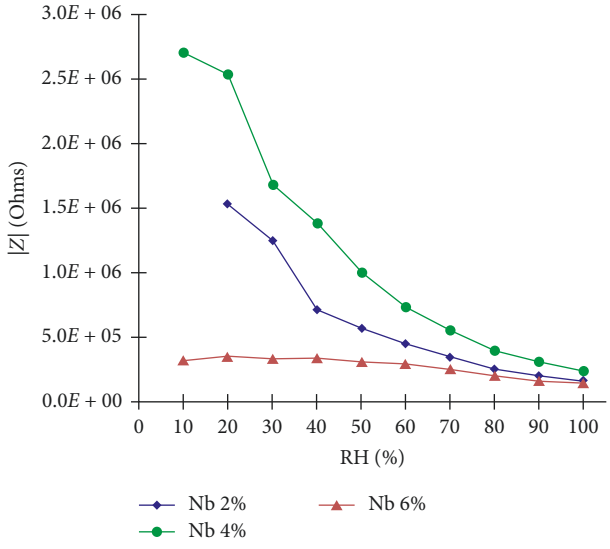

(b)

Figure 6: Impedance change with RH, at 1.3 kHz (a) and 4 kHz (b), at 20°C for all three sensors (it was not possible to calculate values of the impedance modulus for 10% RH in the TiW-Nb2 sensor at 4 kHz).

devices as a function of RH due to the doping level established by the additive.

3.3.1. Electrical Circuit Modelling for Sample's Response. Equivalent circuits have been considered as an interesting source of parameters [25–27] that have been associated with different mechanisms in overall electrical response. The circuit represented in Figure 7 has been explored by the authors in recent works [8, 9], and the components are described below:

C_{geo} is used to represent the geometrical capacitance, while the bulky granular response is assigned to $R_1//C_1$. The grain boundary contribution is assigned to the parallel

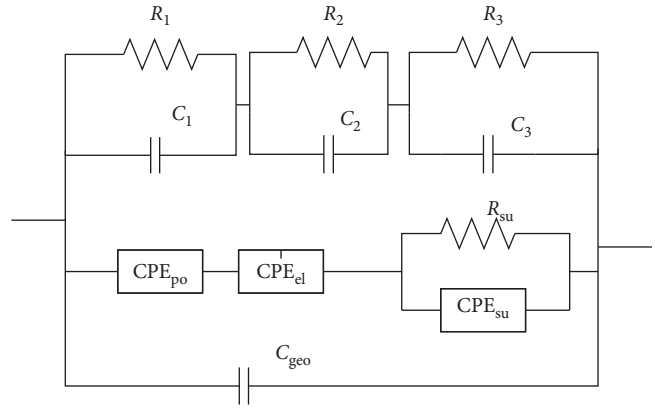

Figure 7: Proposed equivalent circuit for the sensors.

circuit $R_2//C_2$, while the component $R_3//C_3$ characterizes the surface contribution from electron tunnelling along the water layers disposed above the semiconductor surface. The charge diffusion is represented by a constant phase element, CPE [25, 28]. For both referred diffusion mechanisms, the interfacial character of their impedance makes it partly capacitive as well as resistive: CPE_{po} has to do with the contribution of the pores, due to diffusion phenomena taking place inside the water-filled pores, and CPE_{el} is related to the electrode-water layer interface diffusion phenomena that take place at that interface.

In Tables 2–4, the best-fit parameters for the proposed electrical equivalent circuit are summarized. A_{el} and n_{el} represent the two parameters of the impedance CPE_{el}, while A_{po} and n_{po} represent the two parameters of the impedance CPE_{po}.

Due to the strong variation observed in two of these parameters, R_1 and R_2 were chosen as relevant parameters for RH dependence of impedance data.

Figure 8 shows the dependence of R_1 as a function of RH for different doping levels. A general tendency of reduction of the corresponding bulk resistance is observed with increasing RH concentration, as a consequence of progressive diffusion of water molecules into the bulk of the devices. In addition to this, it is possible to identify a niobium-dependent variation of R_1 with RH. The minimal variation is observed for the sample TiW-Nb6, while the maximum one is reached for the sample TiW-Nb4.

The water diffusion in the corresponding structure introduces a competition for transport mechanisms with intrinsic electrical properties. The higher doping level samples are minimally affected by water incorporation, since efficient channels for current transport are established under doping; the water impregnation in the bulk of the samples represents a minimal perturbation in the corresponding transport process. In the opposite direction, for the sample TiW-Nb4, this process is extremely dependent on water incorporation.

The dependence of grain boundary resistance (R_2)—shown in Figure 9—confirms the observed behavior. Maximum variation in R_2 is observed for the sample TiW-Nb4, while negligible variation is observed for the sample TiW-Nb6.

Table 2: Fit parameters for presented Nyquist plots of the sensor TiW-Nb2 at 20°C.

RH (%)	R_1 (Ω)	C_1 (F)	R_2 (Ω)	C_2 (F)	R_3 (Ω)	C_3 (F)	C_{geo} (F)	A_{el} (Ω^{-1})	n_{el}	A_{po} (Ω^{-1})	n_{po}	A_{sup} (Ω^{-1})	n_{sup}	R_{sup} (Ω)
10	6.0E + 5	3.1E − 10	1.89E + 6	1.1E − 11	9.9E + 4	6.0E − 11	1.43E − 11	2.22E − 9	5.2E − 1	6.0E − 9	6.1E − 1	9.0E − 12	9.9E − 1	9.0E + 4
20	4.7E + 5	5.8E − 10	1.93E + 6	1.55E − 11	9.9E + 4	6.0E − 11	1.4E − 11	2.22E − 9	5.16E − 1	6.4E − 9	6.1E − 1	9.0E − 12	9.9E − 1	8.0E + 4
30	3.6E + 5	5.8E − 10	1.47E + 6	1.55E − 11	9.9E + 4	6.0E − 11	1.4E − 11	2.22E − 9	5.2E − 1	6.4E − 9	6.1E − 1	9.0E − 12	9.9E − 1	5.0E + 4
40	6.8E + 5	7.0E − 11	8.30E + 5	8.0E − 12	9.9E + 4	6.0E − 11	1.6E − 12	2.5E − 9	5.18E − 1	3.9E − 9	6.15E − 1	9.0E − 12	9.9E − 1	6.5E + 4
50	5.8E + 5	7.0E − 11	5.80E + 5	8.9E − 12	1.04E + 5	6.0E − 11	2.0E − 12	2.5E − 9	5.3E − 1	3.9E − 9	6.15E − 1	5.47E − 12	9.9E − 1	3.9E + 4
60	4.3E + 5	8.0E − 11	4.00E + 5	8.9E − 12	1.04E + 5	6.0E − 11	2.7E − 12	2.5E − 9	5.4E − 1	3.9E − 9	6.15E − 1	5.47E − 12	9.9E − 1	3.3E + 4
70	3.25E + 5	8.0E − 11	2.57E + 5	8.9E − 12	1.08E + 5	5.0E − 11	2.0E − 12	2.5E − 9	5.43E − 1	3.9E − 9	6.15E − 1	5.47E − 9	5.0E − 1	1.3E + 4
80	2.6E + 5	8.0E − 11	1.70E + 5	8.9E − 12	1.05E + 5	4.7E − 11	8.0E − 13	2.5E − 9	5.43E − 1	6.0E − 9	6.23E − 1	5.47E − 9	5.0E − 1	9.0E + 3
90	2.0E + 5	9.0E − 11	1.27E + 5	8.9E − 12	1.0E + 5	4.7E − 11	5.0E − 13	2.5E − 9	5.45E − 1	6.0E − 9	9.0E − 1	5.47E − 9	5.0E − 1	7.0E + 3
100	1.63E + 5	8.8E − 11	1.07E + 5	8.8E − 12	1.0E + 5	4.7E − 11	3.0E − 13	2.5E − 9	5.53E − 1	6.0E − 9	9.0E − 1	5.47E − 9	5.0E − 1	5.0E + 3

Table 3: Fit parameters for presented Nyquist plots of the sensor TiW-Nb4 at 20°C.

RH (%)	R_1 (Ω)	C_1 (F)	R_2 (Ω)	C_2 (F)	R_3 (Ω)	C_3 (F)	C_{geo} (F)	A_{el} (Ω^{-1})	n_{el}	A_{po} (Ω^{-1})	n_{po}	A_{sup} (Ω^{-1})	n_{sup}	R_{sup} (Ω)
10	2.4E + 6	3.1E − 10	4.52E + 6	1.1E − 11	7.9E + 4	6.0E − 11	2.0E − 11	2.22E − 9	5.45E − 1	6.4E − 9	6.2E − 1	9.0E − 12	9.9E − 1	9.0E + 5
20	2.0E + 6	3.1E − 10	4.08E + 6	1.1E − 11	7.9E + 4	6.0E − 11	2.0E − 11	2.22E − 9	5.45E − 1	6.4E − 9	6.2E − 1	9.0E − 12	9.9E − 1	8.0E + 5
30	9.9E + 5	3.1E − 10	2.35E + 6	1.0E − 11	6.9E + 4	6.0E − 11	1.0E − 11	2.22E − 9	5.4E − 1	6.4E − 9	6.2E − 1	9.0E − 12	9.9E − 1	4.1E + 5
40	9.2E + 5	2.7E − 10	1.8E + 6	9.0E − 12	6.9E + 4	6.0E − 11	1.0E − 11	2.22E − 9	5.4E − 1	6.4E − 9	6.2E − 1	9.0E − 12	9.9E − 1	3.1E + 5
50	7.4E + 5	2.5E − 10	1.25E + 6	9.0E − 12	4.1E + 4	6.0E − 11	1.0E − 11	2.22E − 9	5.4E − 1	6.4E − 9	6.2E − 1	9.0E − 12	9.9E − 1	9.0E + 4
60	5.9E + 5	2.25E − 10	8.47E + 5	9.0E − 12	4.8E + 4	8.0E − 10	1.0E − 11	2.4E − 9	5.4E − 1	6.4E − 9	6.2E − 1	9.0E − 12	9.9E − 1	2.7E + 4
70	4.3E + 5	2.2E − 10	5.8E + 5	8.0E − 12	1.2E + 5	2.7E − 10	9.0E − 12	2.4E − 9	5.4E − 1	6.4E − 9	6.2E − 1	9.0E − 12	9.9E − 1	1.4E + 4
80	1.4E + 5	2.4E − 10	3.75E + 5	7.4E − 12	2.09E + 5	6.8E − 10	1.0E − 11	4.0E − 9	5.4E − 1	2.8E − 9	6.1E − 1	5.0E − 10	8.0E − 1	3.04E + 5
90	1.4E + 5	1.5E − 10	3.0E + 5	7.2E − 12	1.55E + 5	5.6E − 10	7.0E − 12	4.0E − 9	5.4E − 1	2.9E − 9	6.1E − 1	6.0E − 10	8.8E − 1	1.5E + 5
100	9.5E + 4	1.5E − 10	2.2E + 5	7.2E − 12	1.1E + 5	5.0E − 10	7.0E − 12	5.0E − 9	5.4E − 1	2.9E − 9	6.1E − 1	6.5E − 10	8.8E − 1	1.04E + 5

Table 4: Fit parameters for presented Nyquist plots of the sensor TiW-Nb6 at 20°C.

RH (%)	R_1 (Ω)	C_1 (F)	R_2 (Ω)	C_2 (F)	R_3 (Ω)	C_3 (F)	C_{geo} (F)	A_{el} (Ω^{-1})	n_{el}	A_{po} (Ω^{-1})	n_{po}	A_{sup} (Ω^{-1})	n_{sup}	R_{sup} (Ω)
10	1.0E + 5	5.0E − 11	1.81E + 5	6.0E − 11	6.0E + 4	9.0E − 11	3.0E − 11	2.22E − 9	5.45E − 1	6.4E − 9	6.2E − 1	9.E − 11	9.0E − 1	7.0E + 3
20	1.11E + 5	5.0E − 11	2.03E + 5	5.0E − 11	6.0E + 4	9.0E − 11	3.0E − 11	2.22E − 9	5.45E − 1	6.4E − 9	6.2E − 1	9.E − 11	9.0E − 1	7.0E + 3
30	1.01E + 5	3.0E − 11	1.99E + 5	3.0E − 11	6.0E + 4	9.0E − 11	3.0E − 11	2.22E − 9	5.45E − 1	6.4E − 9	6.2E − 1	9.E − 11	9.0E − 1	7.0E + 3
40	9.4E + 4	1.0E − 10	2.72E + 5	4.0E − 11	1.2E + 4	2.0E − 8	2.0E − 11	3.8E − 9	5.55E − 1	2.0E − 9	6.2E − 1	9.E − 11	9.0E − 1	7.0E + 3
50	8.4E + 4	1.0E − 10	2.45E + 5	4.0E − 11	2.4E + 4	7.0E − 9	2.0E − 11	5.0E − 9	5.55E − 1	2.0E − 9	6.2E − 1	9.E − 11	9.0E − 1	7.0E + 3
60	8.5E + 4	1.3E − 10	2.4E + 5	5.0E − 11	5.3E + 4	2.7E − 9	5.0E − 12	4.9E − 9	5.55E − 1	3.0E − 9	6.2E − 1	9.E − 11	9.0E − 1	1.8E + 4
70	5.5E + 4	1.3E − 10	2.1E + 5	3.9E − 11	6.6E + 4	1.4E − 9	3.0E − 12	4.5E − 9	5.58E − 1	3.0E − 9	6.2E − 1	9.E − 11	9.0E − 1	1.4E + 4
80	4.8E + 4	1.3E − 10	1.66E + 5	3.9E − 11	9.3E + 4	7.0E − 10	3.0E − 12	9.0E − 9	5.58E − 1	2.8E − 9	6.2E − 1	1.E − 12	9.0E − 1	2.4E + 4
90	4.8E + 4	1.3E − 10	1.69E + 5	3.9E − 11	8.7E + 4	7.9E − 10	3.0E − 12	8.0E − 9	5.58E − 1	2.8E − 9	6.2E − 1	1.E − 12	9.0E − 1	1.4E + 4
100	4.1E + 4	1.8E − 10	1.17E + 5	3.7E − 11	9.7E + 4	4.8E − 10	1.0E − 12	2.0E − 8	5.58E − 1	2.9E − 9	6.2E − 1	2.E − 11	9.0E − 1	4.1E + 4

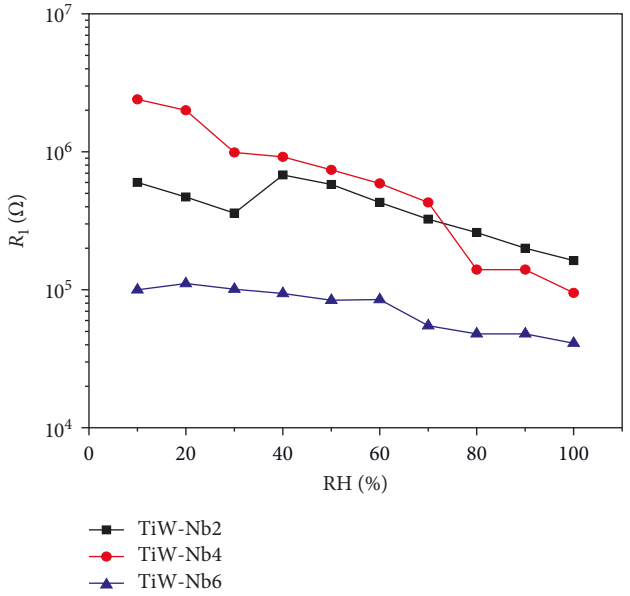

Figure 8: Dependence of R_1—fitting parameter of equivalent circuit with RH variation at different doping levels.

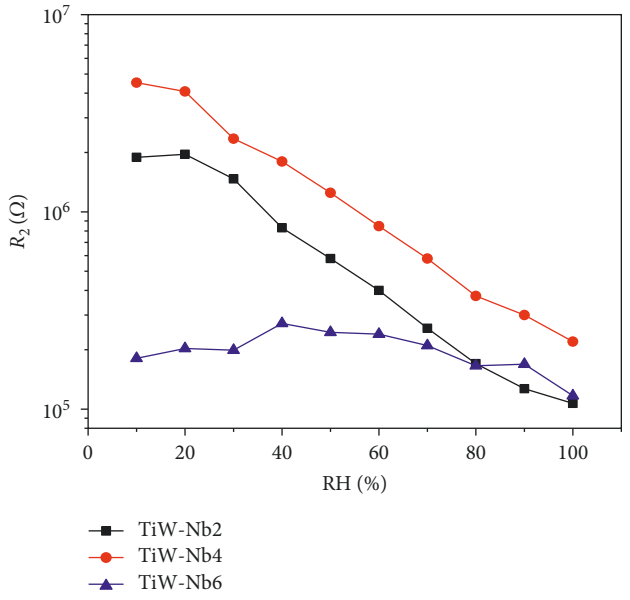

Figure 9: Dependence of R_2—fitting parameter of equivalent circuit with RH variation at different doping levels.

The sensitivity of all three doped samples taken at 1.3 and 4 kHz is plotted in Figure 10. The sensitivity was calculated using the ratio between the conductivity of the sensor exposed to a certain moisture concentration and the conductivity of the sensor under a dry air atmosphere. As can be seen, the sample that exhibits the best sensitivity is the one doped with 4% of niobium, in accordance with the discussed morphology of the resulting material and with the impedance changes with moisture previously discussed.

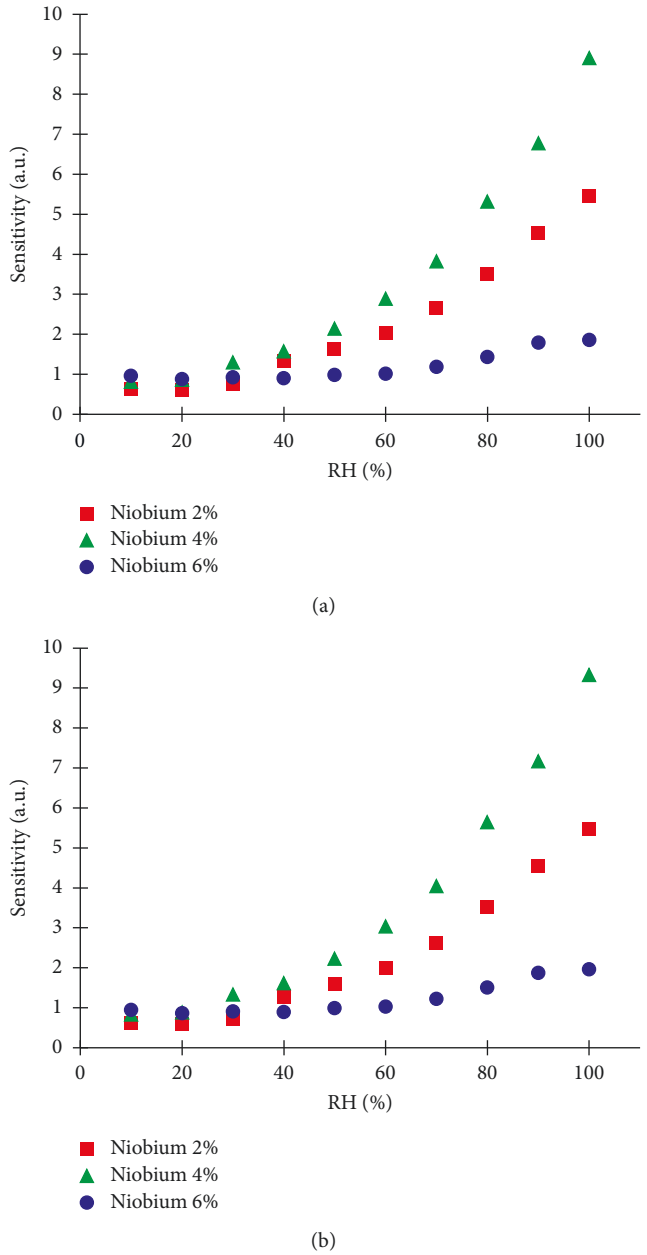

Figure 10: Sensitivity change with RH, at 1.3 kHz (a) and 4 kHz (b), at 20°C for all three sensors.

These results confirm that structural modification provided by niobium returns the best sensibility to RH at 4% of niobium. At this condition, the competition established between the doping level, induced by additive, and electrical response of structure to water layer incorporation is maximized, characterizing an optimal condition for TiW-Nb-based RH samples.

4. Conclusion

The doping level established by Nb_2O_5 in $TiO_2 : WO_3$ composites preserves the anatase phase and provides modifications at the atomic level of the resulting structure (niobium modifies the crystal lattice of titanium) as detected by XRD data.

This induced structural modification requires specific and low concentration of the dopant (sample TiW-Nb4) in order to optimize the RH sensitivity of the resulting composite. Above this critical value, the high conductivity of the obtained devices affects the sensibility degree of the structure, due to the progressive aggregation of grains and higher surface conductivity at low RH condition.

Conflicts of Interest

The authors declare that there are no conflicts of interest regarding the publication of this paper.

References

[1] X. Yu, T. J. Marks, and A. Facchetti, "Metal oxides for optoelectronic applications," *Nature Materials*, vol. 15, no. 4, pp. 383–396, 2016.

[2] L. Alibabaei, H. Luo, R. L. House, P. G. Hoertz, R. Lopez, and T. J. Meyer, "Applications of metal oxide materials in dye sensitized photoelectrosynthesis cells for making solar fuels: let the molecules do the work," *Journal of Materials Chemistry A*, vol. 1, no. 13, pp. 4133–4145, 2013.

[3] A. Umar and Y.-B. Hahn, *Metal Oxide Nanostructures and Their Applications*, American Scientific Publishers, Valencia, CA, USA, 2010.

[4] Z. Chen and C. Lu, "Humidity sensors: a review of materials and mechanisms," *Sensor Letters*, vol. 3, no. 4, pp. 274–295, 2005.

[5] T. Blank, L. Eksperiandova, and K. Belikov, "Recent trends of ceramic humidity sensors development: a review," *Sensors and Actuators B: Chemical*, vol. 228, pp. 416–442, 2016.

[6] H. Farahani, R. Wagiran, and M. N. Hamidon, "Humidity sensors principle, mechanism, and fabrication technologies: a comprehensive review," *Sensors*, vol. 14, no. 5, pp. 7881–7939, 2014.

[7] T. Nenov and Z. Nenova, "Multi-objective optimization of the parameters of TiO_2-based ceramic humidity sensors," *Ceramics International*, vol. 39, no. 4, pp. 4465–4473, 2013.

[8] P. M. Faia, J. Libardi, and C. S. Louro, "Effect of V_2O_5 doping on p- to n- conduction type transition of TiO_2:WO_3 composite humidity sensors," *Sensors and Actuators B: Chemical*, vol. 222, pp. 952–964, 2016.

[9] P. M. Faia, E. L. Jesus, and C. S. Louro, "TiO_2:WO_3 composite humidity sensors doped with ZnO and CuO investigated by impedance spectroscopy," *Sensors and Actuators B: Chemical*, vol. 203, pp. 340–348, 2014.

[10] W.-P. Tai, J.-G. Kim, and J.-H. Oh, "Humidity sensitive properties of nanostructured Al-doped ZnO: TiO_2 thin films," *Sensors and Actuators B: Chemical*, vol. 96, no. 3, pp. 477–481, 2003.

[11] M. Anbia and S. E. M. Fard, "Improving humidity sensing properties of nanoporous TiO_2–10mol% SnO_2 thin film by co-doping with La^{3+} and K^+," *Sensors and Actuators B: Chemical*, vol. 160, no. 1, pp. 215–221, 2011.

[12] M. Anbia and S. M. Fard, "A humidity sensor based on KCl-doped nanoporous $Ti_{0.9}Sn_{0.1}O_2$ thin films prepared by the sol–gel method," *Scientia Iranica*, vol. 19, no. 3, pp. 546–550, 2012.

[13] P. M. Faia and J. Libardi, "Response to humidity of TiO_2: WO_3 sensors doped with V_2O_5: influence of fabrication route," *Sensors and Actuators B: Chemical*, vol. 236, pp. 682–700, 2016.

[14] J. Arbiol, J. Cerda, G. Dezanneau et al., "Effects of Nb doping on the TiO_2 anatase-to-rutile phase transition," *Journal of Applied Physics*, vol. 92, no. 2, pp. 853–861, 2002.

[15] M. Carotta, M. Ferroni, D. Gnani et al., "Nanostructured pure and Nb-doped TiO_2 as thick film gas sensors for environmental monitoring," *Sensors and Actuators B: Chemical*, vol. 58, no. 1, pp. 310–317, 1999.

[16] L. Gan, C. Wu, Y. Tan, B. Chi, J. Pu, and L. Jian, "Oxygen sensing performance of Nb-doped TiO_2 thin film with porous structure," *Journal of Alloys and Compounds*, vol. 585, pp. 729–733, 2014.

[17] H. C. Choi, Y. M. Jung, and S. B. Kim, "Size effects in the Raman spectra of TiO_2 nanoparticles," *Vibrational Spectroscopy*, vol. 37, no. 1, pp. 33–38, 2005.

[18] A. Souza-Filho, V. Freire, J. Sasaki, J. Mendes Filho, J. Juliao, and U. Gomes, "Coexistence of triclinic and monoclinic phases in WO_3 ceramics," *Journal of Raman Spectroscopy*, vol. 31, no. 6, pp. 451–454, 2000.

[19] H. P. de Oliveira, E. G. L. Oliveira, and C. P. de Melo, "Aggregation of methyl orange probed by electrical impedance spectroscopy," *Journal of Colloid and Interface Science*, vol. 303, no. 2, pp. 444–449, 2006.

[20] H. P. de Oliveira, "Determination of pK(a) of dyes by electrical impedance spectroscopy," *Microchemical Journal*, vol. 88, no. 1, pp. 32–37, 2008.

[21] E. S. Araujo, J. Rieumont, C. Nogueiras, and H. P. de Oliveira, "Aggregational processes of low molecular weight polyethylene-b-polyethylene oxide diblock copolymer probed by electrical impedance spectroscopy," *European Polymer Journal*, vol. 46, no. 9, pp. 1854–1859, 2010.

[22] S. V. de Lima and H. P. de Oliveira, "Melting point of ionic ternary systems (surfactant/salt/water) probed by electrical impedance spectroscopy," *Colloids and Surfaces a-Physicochemical and Engineering Aspects*, vol. 364, no. 1–3, pp. 132–137, 2010.

[23] A. A. Al-Amiery, F. A. B. Kassim, A. A. H. Kadhum, and A. B. Mohamad, "Synthesis and characterization of a novel eco-friendly corrosion inhibition for mild steel in 1 M hydrochloric acid," *Scientific Reports*, vol. 6, no. 1, 2016.

[24] E.-M. Köck, M. Kogler, B. Klötzer, M. F. Noisternig, and S. Penner, "Structural and electrochemical properties of physisorbed and chemisorbed water layers on the ceramic oxides Y_2O_3, YSZ, and ZrO_2," *ACS Applied Materials & Interfaces*, vol. 8, no. 25, pp. 16428–16443, 2016.

[25] P. Faia, C. Furtado, and A. Ferreira, "AC impedance spectroscopy: a new equivalent circuit for titania thick film humidity sensors," *Sensors and Actuators B: Chemical*, vol. 107, no. 1, pp. 353–359, 2005.

[26] K. Nitsch, B. Licznerski, H. Teterycz, L. Golonka, and K. Wiśniewski, "AC equivalent circuits of thick film humidity sensors," *Vacuum*, vol. 50, no. 1-2, pp. 131–137, 1998.

[27] A. Tripathy, S. Pramanik, A. Manna et al., "Design and development for capacitive humidity sensor applications of lead-free Ca, Mg, Fe, Ti-oxides-based electro-ceramics with improved sensing properties via physisorption," *Sensors*, vol. 16, no. 7, p. 1135, 2016.

[28] Y. Gönüllü, K. Kelm, S. Mathur, and B. Saruhan, "Equivalent circuit models for determination of the relation between the sensing behavior and properties of undoped/cr doped TiO_2 NTs," *Chemosensors*, vol. 2, no. 1, pp. 69–84, 2014.